Full Paper: TPUs molded at 205 °C, 215 °C and 235 °C are monitored by SAXS and WAXS during straining. A non-affine nanostructure deformation and related evolution mechanisms are found. DSC and microscopy are applied. DSC shows 2 melting endotherms. Results indicate that melts kept below the 2nd peak stay phase-separated. The orientation parameter $f(\varepsilon)$ and $df/d\varepsilon$ from WAXS is related to chain orientation mechanisms (strain ε). SAXS shows hard domains that are only correlated to a next neighbor ("sandwich"). Thick sandwiches lengthen more than thin ones. Thin-layer sandwiches feature a strain limit. Some are converted into thick-layer sandwiches. 2 materials have tough hard domains. Material processed at 235 °C is soft and contains weak hard domains that fail for $\varepsilon > 0.75$.

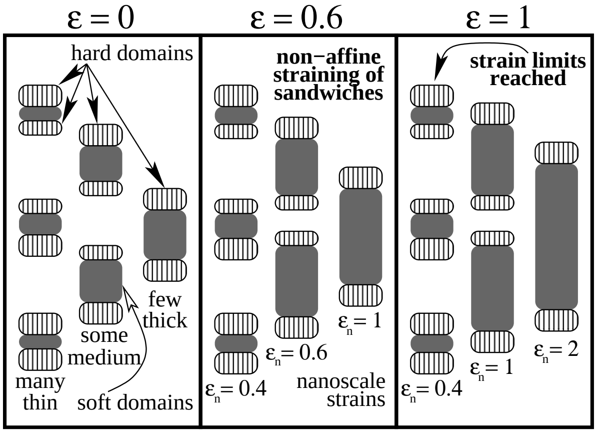

Principal non-affine nanostructure deformation mechanism of hard and soft domains in all TPU samples

Structure and Mechanical Properties of an Injection-Molded Thermoplastic Polyurethane as a Function of Melt Temperature

N. Stribeck[1*], *A. Zeinolebadi*[1], *M. Ganjaee Sari*[1], *A. Frick*[2], *M. Mikoszek*[2], *S. Botta*[3]

[1]Department of Chemistry, Institute of Technical and Macromolecular Chemistry, University of Hamburg, Bundesstr. 45, 20146 Hamburg, Germany. Fax: (+49) 40 42838 6008; E-mail: norbert@stribeck.de
[2]Institute of Polymer Science and Processing, iPSP, Aalen University, Beethovenstr. 1, 73430 Aalen, Germany
[3]HASYLAB at DESY, Notkestr. 85, 22603 Hamburg, Germany

Keywords: elastomers; processing; polyurethanes; small-angle X-ray scattering (SAXS); structure-property relations

1 Introduction

The peculiar rubber elastic properties of thermoplastic elastomers are the consequence of their two- or multi-phase nanostructure consisting of hard domains in a soft matrix. The region of the soft phase between two hard domains is called soft domain. The formation of nanostructure during manufacture is initiated by phase separation, while the polymer melt is cooling down. Phase separation occurs, because the polymer chains are composed from at least two blocks of different chemical composition that are immiscible at the service temperature of the material. Block copolymers synthesized by living polymerization are characterized by uniform block lengths. Processing of such compounds may result in lattice-like nanostructures or even in photonic crystals, in which the soft and the hard blocks reside completely in different domains. This is different with thermoplastic polyurethanes (TPU). Along their chains a mixed sequence of soft segments and hard segments is found. Thus, even optimum process control only leads to domains of very diverse shape and size, the arrangement of which can rarely lead to lattice-like correlation. Moreover, soft domains may contain several hard segments. Consequently, the chemistry[1] and the processing conditions[2,3,4,5] define the nanostructure that, in turn, determines the material's mechanical properties. The hard domains form physical cross-links and make the material behave rubber elastic. Because the hard domains are permanent only to a first approximation, the stress-strain behavior of TPUs is subject to "strong hysteresis, time dependence and cyclic softening".[6] Thus maturing or aging may become a problem, if longer time elapses between investigations with different methods, because in this case the results may not be combined.

Right after the commercial launch of TPUs small-angle X-ray scattering (SAXS) and wide-angle X-ray scattering (WAXS) have been successfully employed to elucidate the structure on the nanometer and sub-nanometer scale by Bonart.[7,1] The materials have been studied in strained and relaxed states, and the recorded two-dimensional (2D) scattering patterns have been analyzed. In the scattering patterns the information on the sequence of hard and soft domains in real space is not contained in the scattering curve that is extracted from the pattern along the straining direction (a slice in the notion of the Fourier-slice-theorem), but in the projection curve of the fiber pattern on the direction of strain. Bonart has pointed out[8] and exploited[1,9,10] this apparently forgotten[11,12] fact. Moreover, in order to avoid a 2D analysis of anisotropic patterns it has become fashionable to reduce it to an isotropic scattering curve by computing circular averages[13] in the raw image, ignoring both the three-dimensionality of reciprocal space and the geometry of the detector plane in reciprocal space. This simple isotropization method is only allowed if two conditions are fulfilled. First, the pattern must be a fiber pattern (uniaxial symmetry). Second, the tangent-plane approximation must be valid – as in SAXS, but not in WAXS.

On the other hand, the technique of X-ray scattering has made considerable progress since the early TPU studies. At that time it was only possible to study samples statically in differently strained states. Today synchrotron sources offer potentials to run complex straining programs[14] and to monitor them simultaneously by 2D SAXS or WAXS with a signal-to-noise ratio that is sufficient for image processing[15] and quantitative analysis.

In this study we do not start from isotropic material like most of the papers do, but start from oriented,[16] injection-molded material that is investigated during a first tensile test. We determine true stress and local strain of the sample at the position of X-ray irradiation. We combine well-known analysis methods that are founded in theory, in order to both avoid systematic errors of heuristic methods, and to attain an almost model-independent view on the structure evolution from the recorded sequences of scattering patterns. In doing so, the focus is on the still little investigated[2,3,4,5] effect of processing conditions on the structure and the properties of the material.

2 Experimental Part

Material. A thermoplastic polyurethane (TPU) is injection molded from melts of different temperature. The material is a commercial grade polyester based thermoplastic polyurethane (TPU) with 94 Shore A durometer hardness from Huntsman Inc., e.g. for sealing applications. The TPU has been polymerized in a one-step process and is provided in granular form ground from cast film. The TPU is composed of MDI (250 g/mol), HQEE (198 g/mol) and Capa (2000 g/mol). The hard segment content is between 45 and 50 wt.-% and has been verified by energy-dispersive X-ray spectroscopy (EDX). The volume fraction of hard segments as estimated from light-microscopy images of microtome cuts has been estimated 34.5 vol.-% yielding a weight fraction of 45 wt.-%.

Injection Molding. Samples for the SAXS measurements have been processed directly from the received material. Thus the corresponding material has first-time been melt processed during injection molding. After processing the samples have been stored for 6 months until the synchrotron beam-time requested for this project had been granted.

Samples for the WAXS measurements have been injection molded from pellets made by extrusion of the received granular material. Thus the TPU material was 2 times melt processed (extrusion / injection molding). Moreover, the WAXS materials had freshly been prepared less than a week before the start of the tensile tests at the synchrotron.

Dumbbell shaped specimens type 5 A according to DIN ISO 527 are injection molded. The nominal dimensions in the central zone of the specimens are 4 mm × 1 mm. Injection molding is carried out in an Arburg 220 S Allrounder 150-30 from pellets dried at 90 °C for 4 h. The screw diameter is 15 mm. Specimens have been molded in a 2-cavity mold and gated with film gate (0.8 mm thick). The mold is kept at a temperature of 60 °C. The injection speed has been set to 25 cm/s where the maximum injection pressure has been 1600 bar. Different kind of samples are produced, the temperature at the nozzle of the injection unit is set to 205 °C, 215 °C and 235 °C, respectively.

Test Bar Characterization. The injection-molded test bars are characterized by optical microscopy and by differential scanning calorimetry (DSC). Light microscopy is carried out in a Zeiss Axioplan 2 equipped with an AxioCam camera. The specimens are cross-sections cut from the centers of the test bars. They are 10 µm thick. Slicing is carried out at -70 °C using a rotary cryo-microtome Leica RM 2165. A Mettler–Toledo DSC 821^{e} is employed. Sample mass is 5.0 ± 0.1 mg. The samples are studied under nitrogen flux, cooled to -100 °C, equilibrated for 2 min, and heated to 280 °C at a rate of 20 K/min.

Tensile Tests. Tensile testing is performed at ambient temperature in a self-made tensile tester.[17] The machine performs symmetric drawing. It is operated at cross-head velocities of 1 mm/min or 2 mm/min for the monitoring of SAXS or WAXS, respectively. Signals from load cell and transducer are recorded during the experiment. The local tensile strain, ε, at the point of sample irradiation is determined. For this purpose fiducial marks are applied to the sample using a rubber stamp. The sample is monitored by a TV-camera. Video frames are grabbed every 10 s and stored together with the experimental data for determination[18] of the local macroscopic strain. Each experiment has been carried out only once. The reason is the considerable effort for the collection and evaluation of the scattering data.

WAXS Measurements. Wide-angle X-ray scattering (WAXS) is performed in the synchrotron beamline A2 at HASYLAB, Hamburg, Germany. The wavelength of the X-ray beam is 0.15 nm, and the sample-detector distance is 125 mm. Scattering patterns are collected by a 2D marccd 165 detector (mar research, Norderstedt, Germany) in binned 1024 × 1024 pixel mode (pixel size: 158.2 µm × 158.2 µm). During the experiments series of scattering patterns are recorded. The cycle-time is 30 s (20 s exposure).

SAXS Measurements. Small-angle X-ray scattering (SAXS) is carried out in the synchrotron beamline A2 at

HASYLAB, Hamburg, Germany. The sample-detector distance is 2488 mm. Data collection is identical to that of the WAXS experiments. The cycle-time is 60 s (50 s exposure).

3 Data Evaluation

Data analysis is carried out by means of own, freely available[19] procedures written in PV-WAVE®.[20]

Tensile Data. The local tensile strain $\varepsilon = (\ell - \ell_0)/\ell_0$ at the point of sample irradiation by the X-ray beam is computed from the initial distance, ℓ_0, of the fiducial marks close to the point of beam-irradiation, and the respective actual distance, ℓ. The local true stress, $\sigma = F/A$, is computed from the force F measured by the load cell after subtracting the force exerted by the upper sample clamp, and $A = A_0/(\varepsilon+1)$, the estimated actual sample cross-section. A_0 is the initial cross section of the central zone of the test bar. The equation assumes conservation of sample volume.

WAXS Patterns. WAXS patterns recorded on the 2D detector during the tensile tests exhibit fiber symmetry. The axis of the tensile tester is oriented exactly perpendicular to the X-ray beam. Thus, it is not necessary to consider fiber tilt[21,22] for the mapping of the detector image into reciprocal space.[23,24,25,26] Our mapping method[26] requires a sample with sharp crystalline reflections. Because the studied samples do not show such reflections, the mapping parameters have been determined from the WAXS pattern of a semicrystalline poly(vinylidene fluoride) sample in the tensile machine employing the known crystallographic data. As a result, the scattering intensity $I(\mathbf{s}) = I(s_{12}, s_3)$ is obtained. s_{12} and s_3 are the equatorial and the meridional component, respectively, of the reciprocal-space scattering vector $\mathbf{s}$, with $|\mathbf{s}| = s = \sqrt{s_{12}^2 + s_3^2} = (2/\lambda)\sin\theta$. s_3 is the fiber axis and parallel to the strain. λ is the wavelength of radiation, and 2θ is the scattering angle. If $I(\mathbf{s}) = I(s,\phi,\psi)$ is expressed in spherical polar coordinates, uniaxial symmetry means that the intensity is no function of the azimuthal angle ψ, i.e. $I(s,\phi)$ with $s_{12} = s\sin\phi$. The spherical inclination angle ϕ is measured with respect to the fiber axis s_3.

For fiber patterns $I(s,\phi)$ that show peaks smeared-out on circular arcs it makes sense to extract slices at fixed $|\mathbf{s}| = s_m$, i.e. $\lceil I(\mathbf{s})\rceil_{s_m}(\phi) = I(s_m,\phi)$. Such slices are a function of the inclination angle ϕ, but are frequently addressed “azimuthal” scans. $g(s_m,\phi,b) = I(s_m,\phi) - b$ is the pole figure of the scattering entities with the correlation distance $d_m = 1/s_m$. Here b is a scattering background that is not related to the sought-after scattering entities, but to other structural[27] effects like Compton scattering, Breit-Wigner recoil factor and to the setup (machine background, read-out noise, dark current, etc.). In this study s_m is chosen from the position of the maximum of the amorphous halo. The halo reflects the distribution and orientation of the inter-chain distances in the polymer.

Orientation can be quantified by the uniaxial orientation parameter[28,29,30]

$$f_{or}(s_m,b) = \frac{\int_0^\pi g(s_m,\phi,b)\,\left[\left(3\cos^2\phi - 1\right)/2\right]\,\sin\phi\,d\phi}{\int_0^\pi g(s_m,\phi,b)\,\sin\phi\,d\phi}, \tag{1}$$

which is the first non-trivial coefficient of the multipole expansion of the fiber-symmetric pole figure $g(s_m,\phi,b)$. In fact, $f_{or}(s_m,b)$ is the dipole moment of the pole figure sliced from the WAXS pattern at s_m. Before it can be computed from experimental data, the curve $I(s_m,\phi)$ must be extrapolated both into the blind wedge around $\phi = 0°$ (meridian), and into the equatorial region around $\phi = 90°$ that is affected by the semitransparent beam stop used. Data are extrapolated by smooth cubic spline functions[31,20] choosing natural smoothing. Assuming $b = 0$ in a first evaluation round, no background is removed. In a second evaluation $b > 0$ is determined by removing the diffuse background that is found to increase with s^2 in the mapped WAXS pattern. Background removal is sketched in Figure 1.

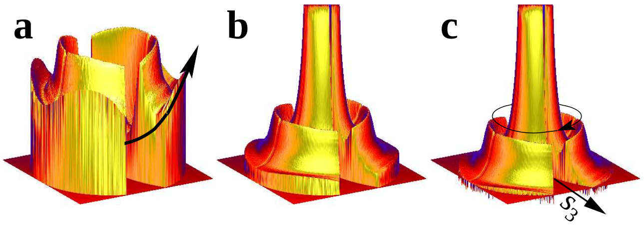

Figure 1: Removal of diffuse background. **a**: WAXS fiber pattern $I(s,\phi)$ mapped into reciprocal space. The arrow indicates diffuse background scattering that increases with s^2. **b**: no more background increase in $I(s,\phi)/s^2$. **c**: $I(s,\phi)/s^2 - c$. c is the constant background in $I(s,\phi)/s^2$. The circular arrow indicates the inclinational intensity slice at $s = s_m$, $I(s_m,\phi)$. It is extracted to determine the orientation of the most probable distance between adjacent polymer chains. s_3 is the meridional axis

The pattern mapped into reciprocal space is shown in Figure 1a. The observed radial (s) background increase with cs^2 is indicated by a curved arrow. Division by s^2 (Figure 1b) makes the background become almost constant, and the minimum intensity is readily subtracted (Figure 1c). When the uniaxial orientation parameter f_{or} is determined from a background-modified pole figure $I(s_m,\phi)/s_m^2 - c$, the absolute value $|f_{or}|$ becomes bigger. We do not claim that the proposed heuristic method is correct. Ruland[27] has expatiated on the required calibration procedures.

Whenever the integral of Equation (1) is computed, the position $\phi = 0$ must be assigned correctly. ϕ is not an azimuthal angle with its origin at the equator, but the inclination angle in spherical coordinates that is measured with respect to the meridian (Cf. Figure 1c). Mixing up[32] the reference direction results in erratic orientation parameter data. By rule-of-thumb, the analysis of arc-shaped reflections on the equator must yield negative values of f_{or}. Peaks centered on the meridian must return positive f_{or}. In the latter case f_{or} cannot be computed with sufficient accuracy directly from the detector image. It is mandatory to prepare the WAXS pattern by, first, mapping it into reciprocal space[26] and, second, filling the blind wedge by extrapolation.

SAXS Patterns. The scattering patterns are transformed into a representation of the nanostructure in real space. The only assumption is presence of a multiphase topology. The result is a multidimensional chord distribution function (CDF), $z(\mathbf{r})$.[33] The method is exemplified in a textbook (Stribeck,[30] Sect. 8.5.5). For a schematic sketch of the steps of data analysis and the extraction of structural parameters from the CDF see for example Figure 2 in Stribeck et al.[34] The method is extracting the topological information on nanostructure (e.g. a two-phase topology, $\rho(\mathbf{r}) \in [\rho_{\text{hard}}, \rho_{\text{soft}}]$, of phases with distinct densities) from 2D SAXS patterns with uniaxial symmetry. The resulting CDF is an “edge-enhanced autocorrelation function”[35,36,37,38] – the autocorrelation of the gradient field, $\nabla\rho(\mathbf{r})$. Thus as a function of ghost displacement $\mathbf{r}$, the multidimensional CDF $z(\mathbf{r})$ shows peaks wherever there are *domain surface contacts* between domains in $\rho(\mathbf{r})$ and in its displaced ghost. The CDF with fiber symmetry in real space, $z(r_{12}, r_3)$, is computed from the fiber-symmetrical SAXS pattern, $I(s_{12}, s_3)$, of multi-phase materials.[33] In the historical context the CDF is an extension of Ruland’s interface distribution function (IDF)[39] to the multidimensional case or, in a different view, the Laplacian of Vonk’s multidimensional correlation function.[40]

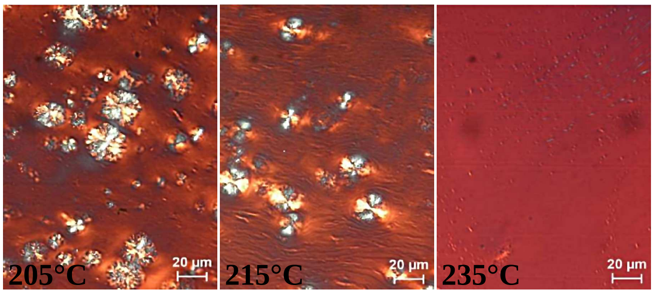

Figure 2: Optical micrographs of cross sections (10 µm thickness, cryo-microtome -70 °C) from the central zone of injection molded test bars. Labels indicate the temperature of the injected melt

4 Results and Discussion

4.1 Test Bar Characterization

Figure 2 presents optical micrographs of the injection-molded materials as a function of the melt temperature. The material manufactured at 205 °C shows a high fraction of spherulitic material. Processed at 215 °C the fraction is considerably lower. In the material made from the hottest melt no spherulites are detected. It is well-known that spherulites grow during polymer crystallization and that they consist of alternating crystalline and amorphous layers. In TPUs the amorphous layers are formed by soft domains, and the hard domains are not completely crystalline, but only quasi-crystalline.[41] This conclusion is drawn because the melt enthalpies of TPUs are generally low.[41,42,43]

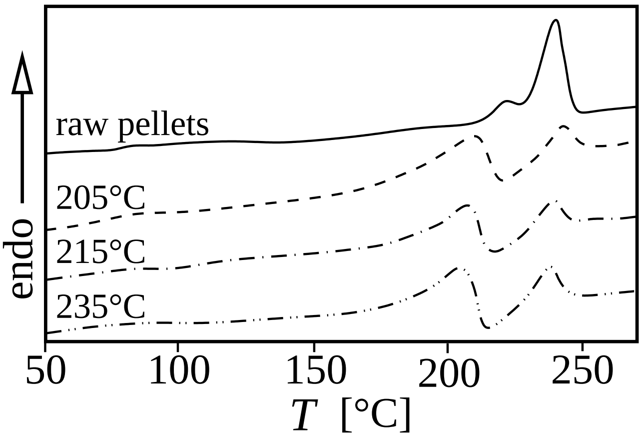

Figure 3: DSC traces of TPU material before (raw pellets) and after injection molding. The labels at the dashed curves indicate the temperature of the injected melt

Figure 3 presents DSC data of the raw pellets and of the injection molded materials. The part between 50 °C and 280 °C is displayed. Below 50 °C the curves are featureless. All samples exhibit two endothermic peaks. They are readily related to the peculiar morphology of thermoplastic polyurethanes. It consists of hard domains in a soft-domain matrix sometimes forming spherulites. The hard domains themselves contain both hard segments and soft segments. Inside the hard domains some proximate hard segments are merged into small crystals. Among the hard segments of the crystals hydrogen bonds are formed. The first endothermic peak has been associated[42] with the melting of these small crystals, the second one has been related[42] to the mixing of hard and soft segments from hard and soft domains to form a single-phase melt. Another explanation for the upper endothermic peak would additionally require the formation of a second crystalline polymorph, as has been reported with non hydrogen-bond forming TPUs.[44] The determined melt enthalpies and melting points are listed in Table 1.

Table 1: Melt enthalpies, ΔH_m and melting temperatures, T_m from the DSC scans in Figure 3. Peak 1 is the low temperature peak. The processed materials are labeled with the temperature of the injected melt

	Peak 1		Peak 2	
sample	ΔH_m [J/g]	T_m [°C]	ΔH_m [J/g]	T_m [°C]
TPU_raw	3.0	211	15.2	237
TPU_205	10.6	207	3.8	240
TPU_215	6.8	206	3.0	239
TPU_235	10.9	202	4.3	237

Uncertainties of the enthalpy determinations are ±0.3 J/g. Melting temperatures have been determined with an uncertainty of ±0.4 K. Considering the processed materials as a function of the injection temperature, ΔH_m does not show a trend. With T_m there is a decrease as a function of increasing injection temperature that indicates a decrease of the average crystallite size.

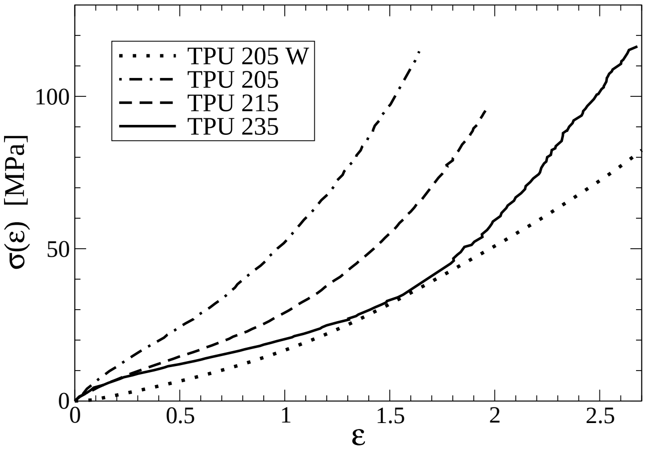

Figure 4: TPU samples strained during the scattering experiments. Stress–strain curve, $\sigma(\varepsilon)$. TPU 205 W indicates the tensile data of the WAXS experiment. The other curves are from the SAXS experiments

4.2 Mechanical Data

The tensile tests in the synchrotron beam have been carried out at constant cross-head speeds of (1 mm/s for SAXS monitoring, 2 mm/s for WAXS monitoring). The stress-strain curves recorded during the experiments are shown in Figure 4. WAXS experiments have been carried out on samples freshly prepared from reprocessed material. In the earlier SAXS tests samples have been used that have been made from manufacturer-supplied crushed granules long time before the measurement. The SAXS tests have stopped when the samples slipped from the clamps. During the WAXS test of TPU 205 the material has started to develop a neck. At this event the experiment has been stopped.

The poor mechanical response during the WAXS test cannot be related to the molding of the testbars, because molding has been identical. There are two possible reasons for the observed differences. Either the reprocessing of used granules has degraded the material, or the WAXS test bars have still been immature. It has been reported that the mechanical properties of the samples may increase considerably within 3 weeks after molding due to improvement of phase separation.

4.3 WAXS TPU 205

Wide-angle X-ray scattering patterns taken during a tensile test of sample TPU 205 are reported in Figure 5. All patterns are on the same linear intensity scale. The fiber patterns are mapped[22,26] into reciprocal space. Wedge-shaped blind regions at the meridian are a consequence of the mapping.[30]

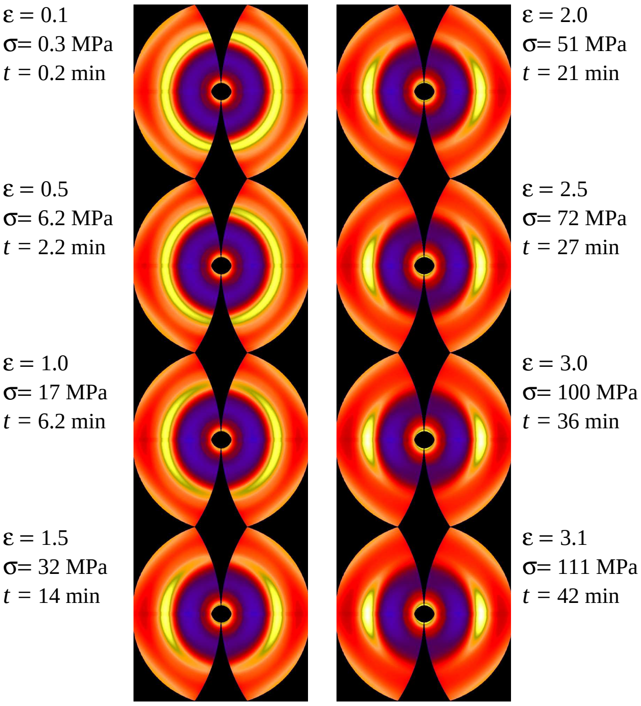

Figure 5: TPU 205. Measured WAXS intensities from the tensile test. Pseudo-color fiber patterns $I(s_{12}, s_3)$ show the region $-3.6\,\mathrm{nm}^{-1} \le s_{12}, s_3 \le 3.6\,\mathrm{nm}^{-1}$. Straining direction ($s_3$) is vertical

On the equator (horizontal, s_{12}-axis) an artificial half-shade originates from the semi-transparent beam stop holder. All patterns exhibit an amorphous halo. With increasing strain the halo becomes more and more anisotropic. Crystalline reflections are not detected with our material, although there are other polyurethanes that show WAXS crystallinity.[3,32] Because polyurethanes vary considerably in chemical composition and morphology, this difference is no contradiction. In order to detect weak crystalline reflections two tests have been performed. First, the WAXS fiber patterns have been isotropized by circular averaging of the mapped patterns and the corresponding curves have been compared to the curves reported by the group of Higgins.[42] Second, the anisotropic fraction of the WAXS pattern has been computed according to the method proposed by the group of Hsiao.[45,46] However, crystallinity cannot be excluded from this result, because tiny crystallites cannot be detected by WAXS. The corresponding reflections are too wide to be distinguished from the amorphous halo.

The angular position of the maximum intensity in the amorphous halo corresponds to a d-spacing of 0.43 nm. This position is identical to the position reported in another TPU study.[3] After not having detected crystallinity with any of the materials nor strain-induced crystallization during the tensile test of TPU 205, tensile tests of the other materials have been skipped.

Figure 5 shows how the WAXS pattern changes during the tensile test. At low strain the amorphous halo appears almost isotropic. With increasing strain the intensity contracts at the equator, finally forming a rather narrow spot. This is expected, because the amorphous halo of the WAXS probes the orientation of the inter-chain gaps that are normal to the chain axes, whereas IR dichroism[47,48,49,50] probes the orientation of chemical bonds that frequently are chosen to directly probe the orientation of the chain axes. Consequently, f_{or} determined from the amorphous halo of the WAXS should be negative, if f_{or} of the chain axes is positive for a material with uniaxial orientation. Without making assumptions there is no way to compute the chain orientation[51,52,53,54,55] from only the orientation of the inter-chain gaps in 3D space.

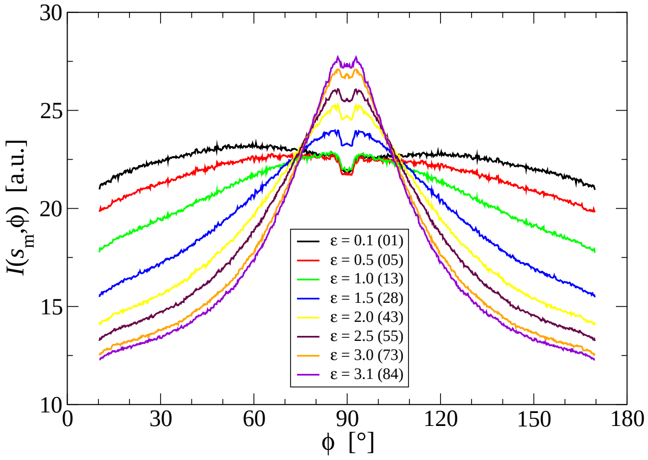

Figure 6: TPU 205. WAXS intensity in the pole figure $I(s_m, \phi)$ cut through the maximum of the amorphous halo at a radius of $s_m = 2.32\,\mathrm{nm}^{-1}$. $\phi = 0$ is on the meridian. Documented in the legend are the strain ε and the index of the X-ray pattern. One index step is 30 s

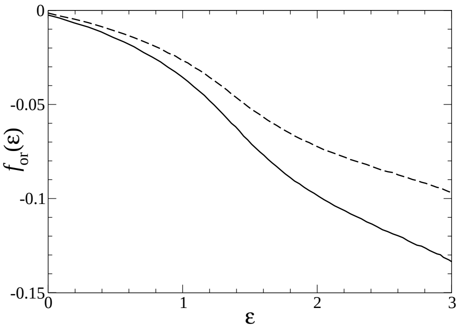

Figure 7: TPU 205. Uniaxial orientation parameter $f_{or}(\varepsilon)$ computed from $I(s_m, \phi)/s_m^2 - c$ (cf. Figure 6). Dashed curve: Without reduction of background scattering, i.e. $c = 0$

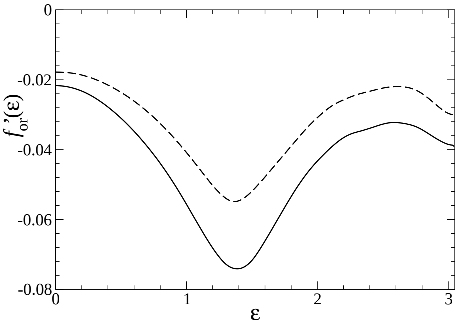

Figure 8: TPU 205. Derivative $f'_{or}(\varepsilon)$ of the uniaxial orientation parameter. Dashed curve: Computed without reduction of background scattering

Figure 6 displays the corresponding inclinational slices through the maximum of the amorphous halo. All curves exhibit an artificial indentation at the equator ($\phi \approx 90°$) originating from the beam stop holder. At low ε anisotropy is demonstrated more clearly in the curves than in the patterns (Figure 5). Up to a strain of $\varepsilon = 0.6$ the amorphous halo is a 4-point pattern with its maxima between meridian and equator. At higher strain the two remnant maxima are on the equator. Because the slices are chosen to cut through the maximum of the amorphous halo, they describe the orientation of the most probable distance among the polymer chains. For a quantitative description of this orientation, the uniaxial orientation parameter, $f_{or}(\varepsilon)$, has been computed as a function of strain ε. Figure 7 shows the result. If the background scattering in the pattern is not reduced (dashed curve), the orientation parameter becomes 30 % smaller than that computed after reduction (solid line), but both curves show the same trend. In terms of f_{or} the initial deviation from isotropy (i.e. $f_{or} = 0$) is small. The ultimate orientation $f_{or}(3) = -0.15$ is still far from the ideal value $f_{or} = -0.5$ of perfect inter-chain gap orientation. Compared to the featureless stress-strain curve of the material (Figure 4), $f_{or}(\varepsilon)$ exhibits an accelerated chain orientation process at medium strain ($1 \leq \varepsilon \leq 2$). We propose to quantify it by the derivative $f'_{or}(\varepsilon) = d\,f_{or}(\varepsilon)/d\varepsilon$ shown in Figure 8. According to the curves, the maximum improvement of inter-chain orientation takes place at $\varepsilon = 1.4$. Unfortunately we cannot relate this process to the results of the SAXS data analysis that follows in the next section, because SAXS and WAXS have been performed after different time with respect to the molding. Consulting the literature and anticipating our results on the general mechanisms of nanostructure evolution, a proposal presented by Bonart[7,48] appears not implausible. According to it the mechanism starts to accelerate the chain orientation after some of the soft domains have reached their strain limit and induce destruction of hard domains. Then the hard segments that are set free respond more easily to the applied load by orientation parallel to the straining direction. Admittedly, for TPUs that show WAXS crystallinity the observed chain orientation may be a superposition of different processes in the hard and in the soft domains, but according to Estes et al.[49] more or less amorphous TPUs exhibit a simple straining mechanism in which the orientation responses of the hard segments and of the soft segments are very similar.

A second process of orientation improvement starts at $\varepsilon \approx 2.7$. This process initiates necking of the sample, which is detected at $\varepsilon = 3$. In the experiment the part of the material that is irradiated by the X-ray beam is far from the neck. As the neck starts to propagate, the material in the irradiated volume begins to shrink. The maximum strain reached in the irradiated volume is $\varepsilon = 3.04$. Thereafter the test is stopped.

4.4 Measured SAXS

Representative SAXS patterns taken during straining experiments of 3 TPU materials are shown in Figure 9 – Figure 11. Remarkably, the nanostructure of all the materials shows considerable orientation already before the mechanical test, whereas the orientation of the WAXS patterns before the test is very low for all materials.

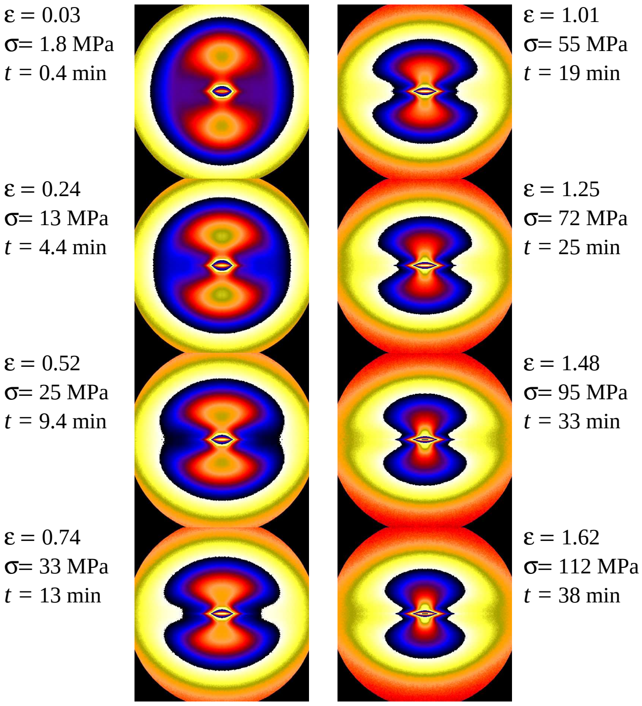

Figure 9: TPU 205. Measured SAXS intensity during the tensile test. The pseudo-color fiber patterns $I(s_{12}, s_3)$ show the region $-0.2\,\mathrm{nm}^{-1} \le s_{12}, s_3 \le 0.2\,\mathrm{nm}^{-1}$. Pattern intensities on a logarithmic scale. Cross-head speed is 2 mm/s. Straining direction is vertical

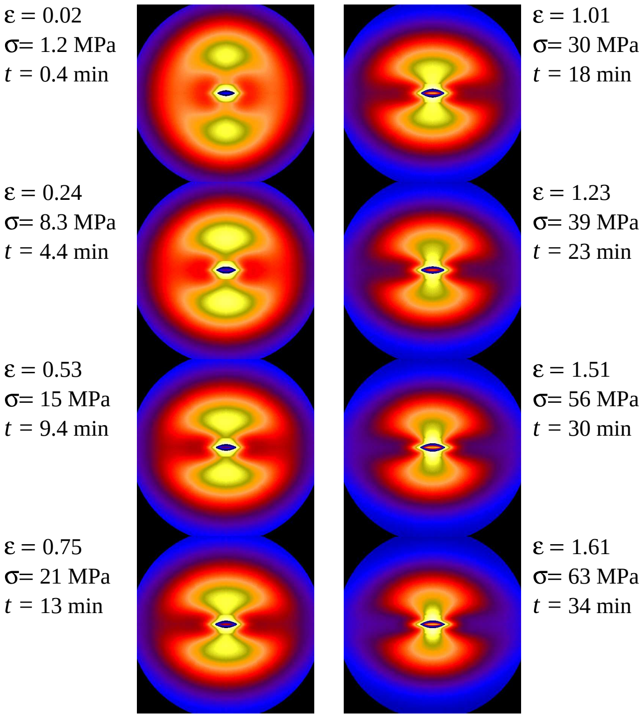

Figure 10: TPU 215. Measured SAXS intensity during the tensile test. The pseudo-color fiber patterns $I(s_{12}, s_3)$ show the region $-0.2\,\mathrm{nm}^{-1} \le s_{12}, s_3 \le 0.2\,\mathrm{nm}^{-1}$. Pattern intensities on a logarithmic scale. Cross-head speed is 1 mm/s. Straining direction is vertical

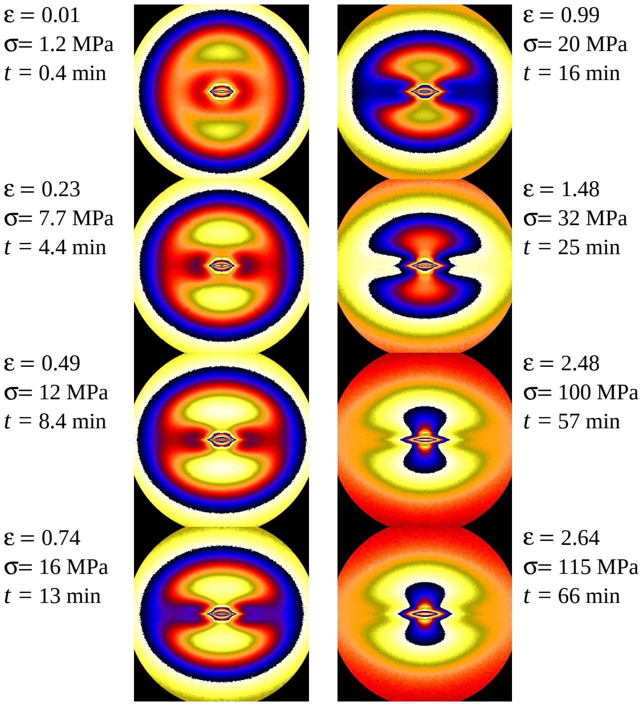

Figure 11: TPU 235. Measured SAXS intensity during the tensile test. The pseudo-color fiber patterns $I(s_{12}, s_3)$ show the region $-0.2\,\mathrm{nm}^{-1} \le s_{12}, s_3 \le 0.2\,\mathrm{nm}^{-1}$. Pattern intensities on a logarithmic scale. Cross-head speed is 1 mm/s. Straining direction is vertical

The intensity scales of the patterns in the figures are identical. All patterns are scaled logarithmically. The tough, mature test bars used in the SAXS experiments have slipped from the clamps after having been exposed to a stress $\sigma \approx 100$ MPa.

Figure 9 shows the scattering patterns taken during the straining of sample TPU 205 that had been injection molded from a melt of 205 °C. The lateral extension of the reflections is broad from the beginning, indicating that the arranged hard domains do not exhibit the shape of extended lamellae, but only of moderately anisotropic domains that arrange to form microfibrils.[56,57,58] With increasing strain an increase of the reflection intensity is observed until $\varepsilon \approx 0.25$. Thereafter the reflection intensity is decreasing. During the test the maximum position of the reflection is moving towards the center of the pattern indicating an increasing distance between the hard domains.

Figure 10 shows selected SAXS patterns from the monitoring of the material that has been injection molded from a melt of 215 °C. A microfibrillar nanostructure with increasing distance between the hard domains is observed. The reflection intensity maximum is first increasing with increasing strain (up to $\varepsilon \approx 0.5$). Thereafter it is decreasing.

Figure 11 shows selected SAXS patterns from the monitoring of the material that has been injection molded from a melt of 235 °C. A microfibrillar nanostructure with increasing distance between the hard domains is observed. The reflection intensity maximum is first increasing with increasing strain (up to $\varepsilon \approx 0.7$). Thereafter it is decreasing.

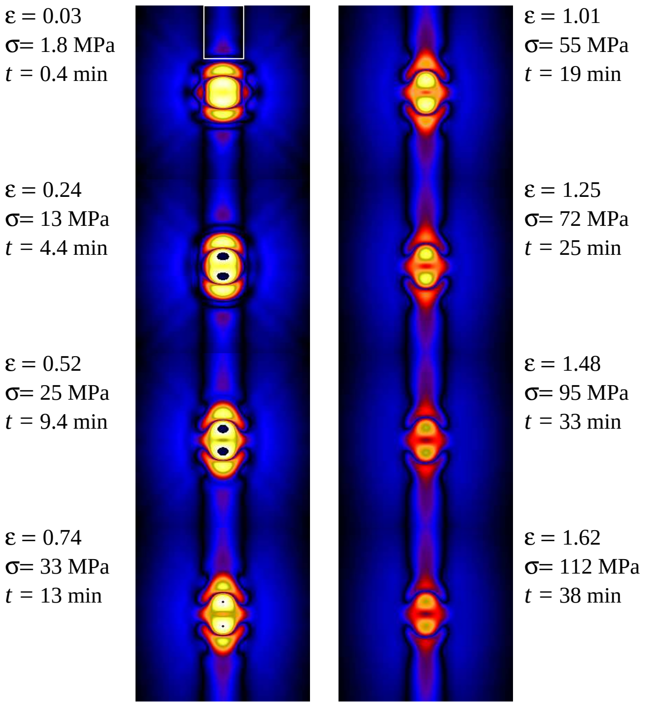

Figure 12: Tensile test of TPU 205. Chord distribution functions (CDF) computed from SAXS. The pseudo-color fiber patterns $|z(r_{12},r_3)|$ show the region $-50\,\mathrm{nm} \le r_{12}, r_3 \le 50\,\mathrm{nm}$. Straining direction is vertical. Pattern intensities on a logarithmic scale. Crosshead speed is 2 mm/s. A white border indicates the region used in Figure 18–20

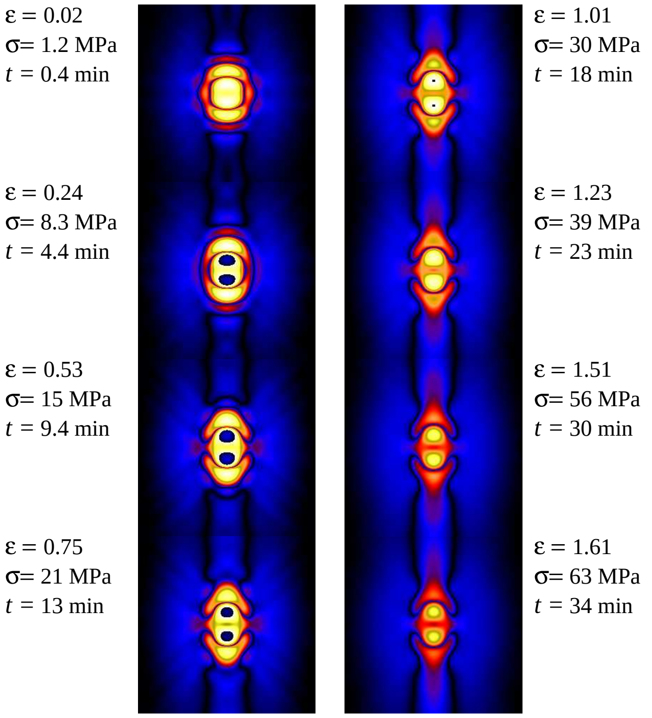

Figure 13: Tensile test of TPU 215. Chord distribution functions (CDF) computed from SAXS. The pseudo-color fiber patterns $|z(r_{12},r_3)|$ show the region $-50\,\mathrm{nm} \le r_{12}, r_3 \le 50\,\mathrm{nm}$.. Straining direction is vertical. Pattern intensities on a logarithmic scale. Crosshead speed is 1 mm/s

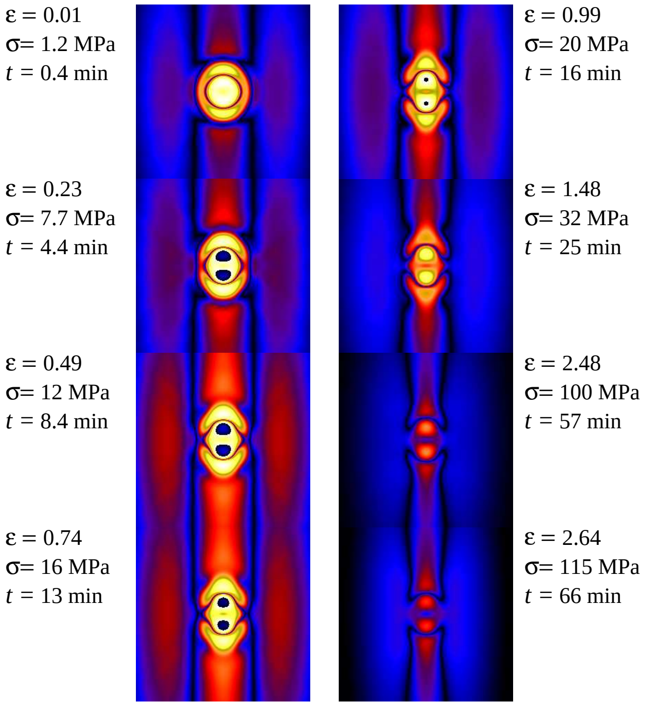

Figure 14: Tensile test of TPU 235. Chord distribution functions (CDF) computed from SAXS. The pseudo-color fiber patterns $|z(r_{12},r_3)|$ show the region $-50\,\mathrm{nm} \le r_{12}, r_3 \le 50\,\mathrm{nm}$. Straining direction is vertical. Pattern intensities on a logarithmic scale. Crosshead speed is 1 mm/s

4.5 CDF: Nanostructure in Real Space

Multidimensional chord distribution functions[33,30] (CDF) visualize the nanostructure of the studied materials and its evolution in real space. While the measured SAXS intensity peaks accentuate the well-correlated domains, the peaks in the CDF are weighted according to the number distribution of domain distances. The results are presented in Figure 12 – Figure 14. The general course of the peak intensities in the CDFs is identical to the development observed in the SAXS patterns. The materials exhibit an initial increase of peak intensities that is followed by a decrease for higher strain.

Already in the unstrained materials the CDF peaks are only moderately extended in horizontal direction, which is the direction perpendicular to the strain. This means that the corresponding hard domains show only a moderate lateral extension that decreases somewhat with increasing strain. Thus the hard domains cannot be addressed “lamellae” from the beginning, but only “anisotropic granules” that degrade with increasing strain becoming less and less extended. This is the well-known transition process from layer stacks to microfibrillar stacks.[57,58] A presentation and discussion of the corresponding analysis would lengthen the paper without adding interesting information.

Figure 12 shows selected CDFs from the monitoring of the material that has been injection molded from a melt of 205 °C. A clean microfibrillar nanostructure with increasing distance between the hard domains is observed. Only few peaks are noticed on the meridian. Because there is no peak outside a distance of 50 nm, the correlation distance among the hard domains is lower than 50 nm. The peaks exhibit a peculiar skewed shape. Moreover, at low strain an x-shaped weak background modulation is observed. This feature is of very low intensity and could be considered a Fourier transform artifact, but during the test it shows a monotonous decrease, and this decrease is closely related to the WAXS observation of the 4-point orientation of the amorphous halo (cf. Figure 6 and Figure 5). When the WAXS maxima have merged on the equator, the x-shaped background peaks in the SAXS CDF have vanished.

Figure 13 shows selected CDFs from the monitoring of the mechanical test of sample TPU 215, the material injection molded from a melt of 215 °C. Similar to TPU 205 a x-pattern background is observed that is visible up to a strain $\varepsilon = 1.3$. As with the TPU 205 the domain peak intensity of the material first increases after the start of the straining (developing dark spots in the center of the peaks) and falls below the initial value as the x-pattern is erased. Similar to TPU 205 the tough material slips from the clamps rather early.

Figure 14 presents the nanostructure evolution during the mechanical test for the material injection molded from the hottest melt (235 °C). A plain microfibrillar pattern is observed from the beginning. No x-pattern background is observed. During the test the microfibrils narrow (vertical bar-shaped reflections move closer to the meridian), and the intensity in the central meridional streak is changing. The simple-minded nanostructure and its response to strain is not observed. This response would not exhibit a meridional streak, but distinct peaks along the meridian that clearly move outward with increasing strain. In all other polymer materials that our group has studied in straining tests so far we have observed such distinct peaks moving. They indicate a well-defined preferential distance between hard domains instead of an extremely broad distribution of distances. Nevertheless, let us relate the position of the peak maximum on the meridian of the CDF to its initial position and discuss it. Is this quantity an adequate measure for a nanoscopic strain with the studied segmented TPU material?

4.6 Macroscopic and Nanoscopic Strain

Figure 15 – 17 present the macroscopic and nanoscopic strains in the irradiated volume of the samples TPU 205 – TPU 235 as a function of elapsed time. ε is the macroscopic strain as computed from the strain of the grid of fiducial marks on the samples. $\varepsilon_{n,I(s)}$ is a nanoscopic strain that is computed from the movement of the maximum position of the SAXS peak in the pattern $I(\mathbf{s})$. $\varepsilon_{n,CDF}$ is a nanoscopic strain parameter computed from the movement of the maximum position of the long-period peak in the CDF. Choosing this parameter we take the most probable long period for the average long period.

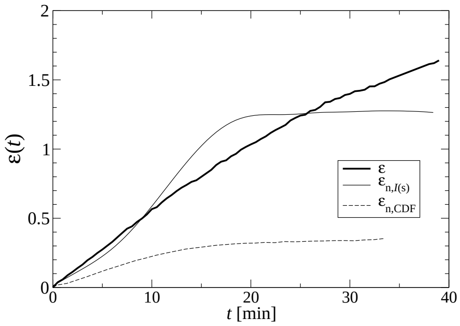

Figure 15: TPU 205. Evolution of strains in the tensile test. ε: macroscopic strain, $\varepsilon_{n,I(s))}$: nanoscopic strain from the shift of the SAXS peak maximum, $\varepsilon_{n,CDF}$: nanoscopic strain from the position of the CDF peak maximum

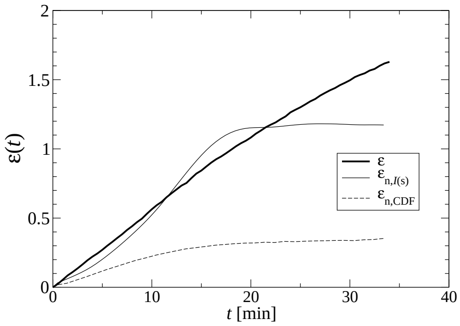

Figure 16: TPU 215. Evolution of strains in the tensile test. ε: macroscopic strain, $\varepsilon_{n,I(s))}$: nanoscopic strain from the shift of the SAXS peak maximum, $\varepsilon_{n,CDF}$: nanoscopic strain from the position of the CDF peak maximum

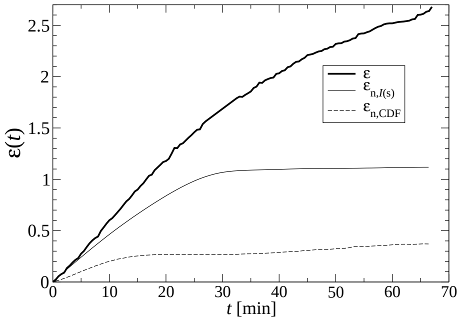

Figure 17: TPU 235. Evolution of strains in the tensile test. ε: macroscopic strain, $\varepsilon_{n,I(s))}$: nanoscopic strain from the shift of the SAXS peak maximum, $\varepsilon_{n,CDF}$: nanoscopic strain from the position of the CDF peak maximum

Obviously, ε and $\varepsilon_{n,I(s)}$ exhibit initially the same behavior for the materials TPU 205 and TPU 215. In TPU 235 $\varepsilon_{n,I(s)}$ is always smaller than the macroscopic strain. For high macroscopic strains the nanoscopic strain from the SAXS peak position, $\varepsilon_{n,I(s)}$, remains constant on a plateau. The structural reason for this strange behavior is found in the CDF. As a first test, the nanoscopic strain $\varepsilon_{n,CDF}$ has been computed. The result appears even stranger. $\varepsilon_{n,CDF} \ll \varepsilon_{n,I(s)}$ is valid throughout the whole experiment, but the onset of the plateau is similar. This finding appears less surprising, if the peak maximum position is no approximation of the mean (the average long period). This is the case, if the long-period distribution is not affinely expanded, but its skewness is growing during the mechanical test.

4.7 Long-period peaks in the CDF: Analysis of Peak Shape

The simple CDF long-period-peak (L-peak) analysis presented in the previous section hooks the maximum of the long-period distribution (brightest area in Figure 18-20), tracks its movement and relates it to a nanoscopic strain $\varepsilon_{n,CDF}$. This approach is only reasonable, if the distribution of the long periods is affinely expanded in the straining experiment. Instead, if the skewness of the distribution is increasing, then $\varepsilon_{n,CDF}$ as computed from the L-Peak *maximum* hangs behind the *average* nanoscopic strain considerably.

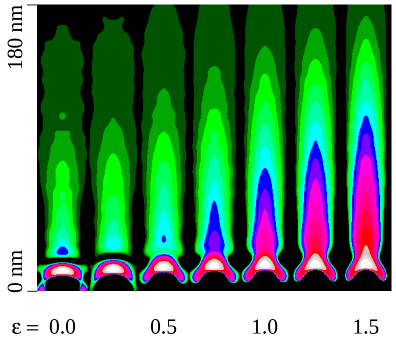

Figure 18: TPU 205. Detail of the CDF: Evolution of the long period peak in real space as a function of macroscopic strain ε. Direction of strain (r_3) is vertical. The width of each band in transverse direction (r_{12}) is ±16 nm

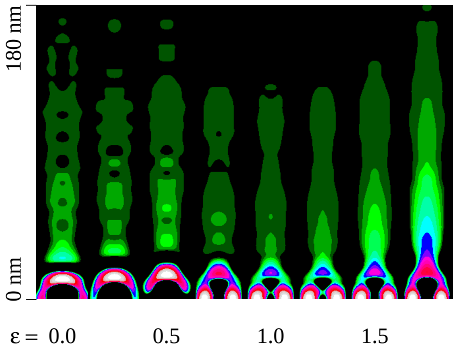

Figure 19: TPU 215. Detail of the CDF: Evolution of the long period peak in real space as a function of macroscopic strain ε. Direction of strain (r_3) is vertical. The width of each band in transverse direction (r_{12}) is ±16 nm

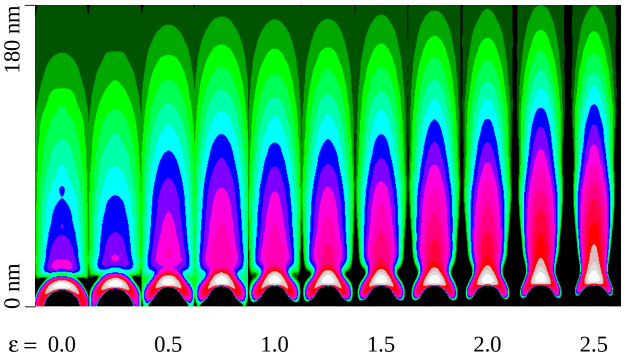

Figure 20: TPU 235. Detail of the CDF: Evolution of the long period peak in real space as a function of macroscopic strain ε. Direction of strain (r_3) is vertical. The width of each band in transverse direction (r_{12}) is ±16 nm

4.7.1 Demonstration of L-Peak Shape Variation

In order to discuss the shape evolution of the long period distributions, the regions (example: white border in Figure 12) of the corresponding peaks are extracted from the CDFs. These regions are collected as a function of ε and displayed in Figure 18 – 20 for discussion.

For sample TPU 205 Figure 18 presents the regions of the L-peak in the CDFs as a function of strain. Here and with sample TPU 235 (Figure 20) the most simple evolution is observed: Upon straining the relative asymmetry of the long period distribution increases considerably: The many thin soft domains are relatively hard, the thick soft domains are considerably softer.

> We do not discuss this disproportionating in terms of different Young's moduli, because there might as well be a different reason: an elastic limit due to full extension of taut tie-molecules that is increasing more or less continuously with increasing soft-layer thickness. Taut tie-molecules may simply block further extension of respective sandwiches.

So the thin soft domains undergo a low nanoscopic strain, whereas the thick soft domains are easily elongated during the straining experiment. When the plateau of $\varepsilon_{n,CDF}(t)$ is reached in Figure 15 – 17, there is no more movement of the maximum position of the L-peak. The many hard soft-domains that contribute to this peak have all reached their elastic limit, whereas the soft domains collected in the tail of the L-peak are still lengthening as a consequence of the continued macroscopic load. Let us consider the widths of the strip-shaped reflections. The widths are a measure of the average hard-domain widths. It is decreasing with increasing macroscopic strain. This indicates disruption of hard domains under stress. This observation supports the chain orientation process by Bonart[7,48] that has been discussed with the WAXS analysis. With TPU 235 the initial width of the hard-domain distribution is wider than with the materials molded from cooler melts.

Figure 19 shows a more complex nanostructure. Here the thickness distribution of the soft domains is not unimodal, but multimodal with several preferential soft domain thicknesses. Nevertheless, even this sample follows the basic mechanism discussed with the other materials. Thin soft domains are harder than thick ones, and the straining of thick domains is easier than the straining of thin domains.

4.7.2 Principal Deformation Mechanism

These results are summarized in a simple sketch (Figure 21) that describes the principal deformation mechanism of the studied TPU materials – still neglecting domain formation, transformation or destruction. The virgin injection-molded material (Figure 21a, $\varepsilon = 0$) exhibits a nanostructure of hard and soft domains with poor inter-domain correlation. Thus the SAXS only sees uncorrelated "sandwiches", e.g. two hard domains with a soft domain in between (or two soft domains with a hard domain in between).

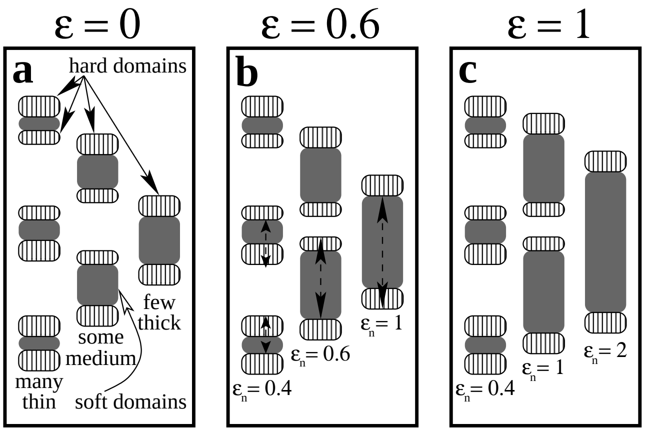

Figure 21: Principal straining mechanism of the studied TPU material. **a**: Unstrained state. There are many sandwiches with thin soft layers and few with thick soft domains. The thicker the soft domains are, the lower is their modulus. **b**: Medium strain. For the thin layers there is a stretching limit. Double-head arrows indicate the distances between phase boundaries that are collected in the L-peak of the CDF. **c**: High strain. Only the medium and thick layer sandwiches keep responding

In the sketch only one type of sandwich is drawn. Thus the main scattering effects in the CDF on the meridian are the domain peak (at very small r_3), and the long period peak (L-peak) that has been discussed in the previous section. By definition of the CDF, the L-peak collects the number-probabilities of those distances between phase boundaries that are indicated by vertical double-head arrows. Inspection of the L-peaks of the unstrained material has yielded that the long period distributions are highly anisotropic. We see many sandwiches with thin soft domains, but few sandwiches with thick soft domains. Figure 21b sketches a situation in the elongated state with changed shape of the sandwiches. We assume that the hard-domain distributions are much more rigid than the soft-domain distributions. Thus from the highly non-affine shape change of the L-peak we infer that change is mainly caused from the straining of soft domains. We observe that the many thin-layer sandwiches are strained ($\varepsilon_{n,CDF}$) much less than the macroscopic strain (ε). On the other hand, the tail of the anisotropic L-peak is extended so far out that the few thick-layer sandwiches have been strained much more than the macroscopic strain. Finally, in Figure 21c, all the thin-layer sandwiches have reached their elastic limit and do not extend any more. Further nanoscopic strain is only taking place in medium-layer and thick-layer sandwiches.

4.7.3 Domain Formation, Transformation and Destruction

As the last step in nanostructure evolution analysis we are searching for hints concerning the formation, transformation and destruction of domains. Initial strain may arrange hard segments in such a way that they form new hard domains. Further straining may break intermediate hard domains, resulting either in a transformation of thin-layer sandwiches into thick-layer sandwiches or in a complete loss that decreases the number of sandwiches.

In order to answer this question we study meridional slices $\lceil z(\mathbf{r}) \rceil_1 (r_3) = z(r_{12} = 0, r_3)$ of the CDF. It appears worth to be noted that such slices in real space, $\mathbf{r}$, describe the correlation among the phase boundaries between hard and soft domains in the direction of strain. If one would like to study the related nanostructure directly in the scattering pattern $I(\mathbf{s})$, one would have to analyze[59,30] the one-dimensional projection curve $\{I(\mathbf{s})\}_1 (s_3) = 2\pi \int s_{12} I(s_{12}, s_3)\, ds_{12}$ in $\mathbf{s}$-space, instead of the frequently studied slice $I(s_{12} = 0, s_3)$. The relation is known as the Fourier slice theorem and has already been pointed out in the early work of Bonart[8,9] on TPUs.

Assuming that there is no relevant correlation beyond the intra-sandwich ones, the curve $-z(r_{12} = 0, r_3)$ cut from the CDF on its meridian must be positive for $r_3 > r_{mt}$. r_{mt} is the maximum thickness of a single domain. Then – apart from oscillations that demonstrate the limit of the assumption – $-z(0, r_3)$ is the distribution of long periods in the material. The strip-plots (cf. Figure 18 – Figure 20) appear to suggest that an analysis might be possible at least to a first approximation. Because of the fact that the scattering patterns have been normalized for constant thickness, the curves can be compared relative to each other.

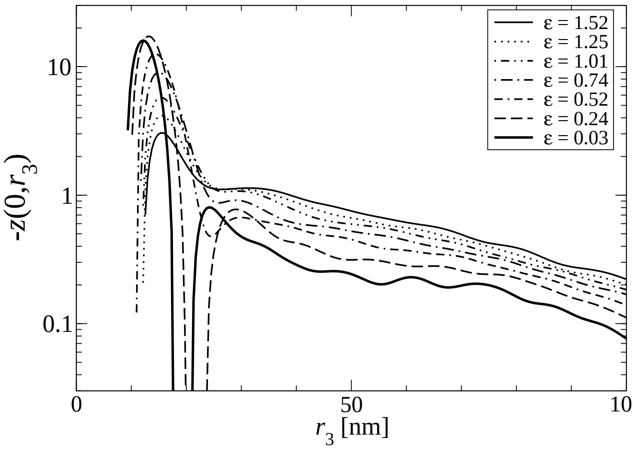

Figure 22: TPU 205. Evolution of CDF slices $-z(r_3)$ along the meridian as a function of macroscopic strain ε

Figure 22-24 show the CDF slices in semi-logarithmic plots. The curves are selected in steps of $\Delta\varepsilon \approx 0.25$. Intensity collapses indicate correlations among neighbors that are violations of the simplifying assumption. Above a level of strain that depends on the sample preparation these collapses become rather small. The thin-layer sandwiches are indicated by the sharp maximum at the beginning of the L-peak.

For all materials the nanostructure shows a broad variety of scattering entities ranging from thin-layer sandwiches to thick-layer sandwiches. After the start of the experiment the thin-layer-sandwich maximum is increasing. Thus the number of thin-layer sandwiches is increasing for TPU 205 and TPU 215 up to $\varepsilon \approx 0.25$, and for TPU 235 up to $\varepsilon \approx 0.5$. An increase of contrast between the hard phase and the soft phase could cause the same effect, but it appears unlikely to assume that the soft-domain density decreases as a result of applied strain. The more probable formation of thin-layer sandwiches may be the result of disruption of clusters of hard-domains that contain soft segments (cf. Figure 25, middle row).

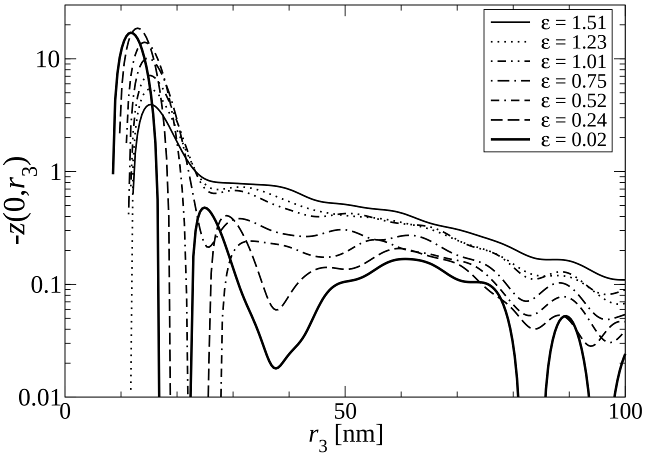

Figure 23: TPU 215. Evolution of CDF slices $-z(r_3)$ along the meridian as a function of macroscopic strain ε

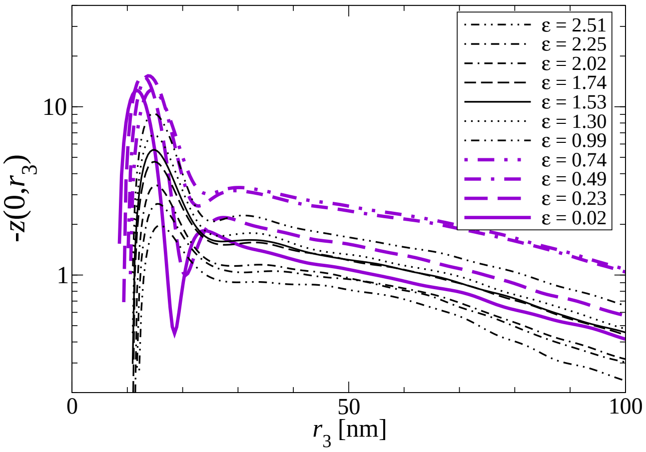

Figure 24: TPU 235. Evolution of CDF slices $-z(r_3)$ along the meridian as a function of macroscopic strain ε

After this initial strain-induced formation of thin-layer sandwiches the number of thin-layer sandwiches is decreasing. For the samples TPU 205 and TPU 215 at the same time the number of sandwiches in the tail of the L-distribution is increasing. Because it is unlikely that at the same time one of the soft phases becomes more dense and the other becomes less dense, this observation shows that some of the thin-layer sandwiches are disrupted and, after that, the remnant hard domain may become member of a thick-layer sandwich. This transformation process is active up to a macroscopic strain $\varepsilon \approx 1.6$. Then the two materials have become so hard that they slip from the clamps of the tensile tester.

For sample TPU 235 the transformation process is only dominant until $\varepsilon \approx 0.75$ (highest curve for $r_3 > 30$ nm). After that even the number of thick-layer sandwiches starts to decrease, most probably because of destruction of their hard domains. As a result, the material appears more soft than TPU 205 and TPU 215. It can be strained until $\varepsilon = 3.1$ before the stress increases beyond 100 MPa and the sample slips from the clamps, as well. Thus we observe a direct correlation between macroscopic properties and the stability of the hard domains controlled by choice of the processing temperature. The detected nanostructure evolution mechanisms are sketched in Figure 25.

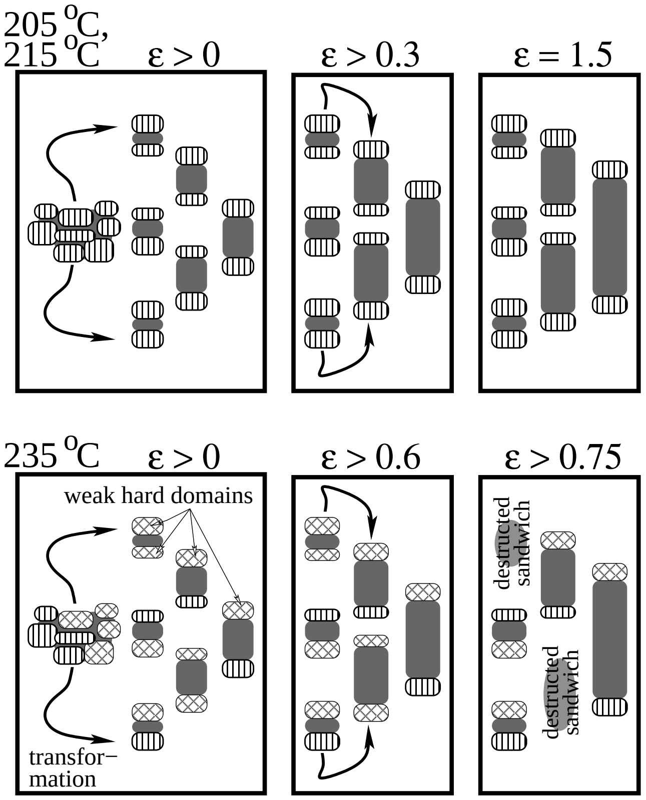

Figure 25: Nanostructure evolution mechanisms of the TPU injection-molded samples as a function of processing temperature and strain

Samples processed from a lower temperature melt (205 °C, 215 °C) exhibit an evolution with two transformation mechanisms among the scattering entities (in the sketch indicated by arrows): At strains $\varepsilon < 0.3$ clusters are transformed into thin-layer sandwiches. Above $\varepsilon > 0.3$ the dominant transformation process is destruction of hard domains from thin-layer sandwiches that leads to an increase of thick-layer sandwiches. The hard domains are strong. The material slips from the clamps at $\varepsilon \approx 1.6$.

The sample processed at 235 °C exhibits an evolution with 3 transformation mechanisms. Only the third one is new: Many hard domains are weak and are destructed during straining. The destruction becomes dominant at $\varepsilon = 0.75$. An explanation for the different hard-domain strengths becomes obvious, because 235 °C is in the center of the second melting endotherm (cf. Figure 3) that has been related to homogeneous mixing[42] of soft and hard segments. The detected strength of hard domains after low-temperature processing may be caused from the fact that phase separation in the mold advances to a higher level when it is applied to a presorted melt. Thus it may be favorable to partially preserve the phase separation between hard and soft segments in the manufacturing process, if the aim is production of TPU materials with strong hard domains.

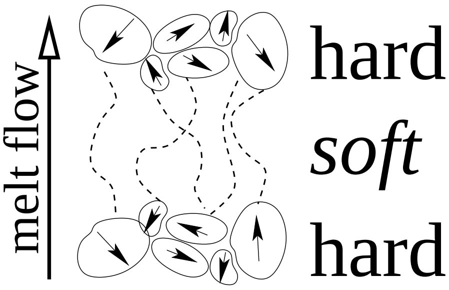

Figure 26: Proposed inner sandwich structure: Hard domains from almost randomly oriented very small grains (that may be crystalline) are preferentially oriented perpendicular to the flow direction of the injected melt. Small arrows indicate the chain orientations inside the grains

Figure 26 shows a model for the initial inner structure of the hard domains that conforms with both the WAXS and the SAXS results. According to this model the hard domains are clusters of very small grains that may be crystalline. SAXS shows that the hard domains as a whole are oriented more or less perpendicular to the melt-flow direction during injection molding. The amorphous halo of WAXS probes the distance distribution between neighboring chains. The result shows that chain orientation directions from the ensemble of grains is almost random. SAXS shows that during the straining process the hard domains break apart, and WAXS shows that the orientation of the grains in the fragments improves.

The materials from the lower injection temperatures contain bigger crystallites inside the hard domain lamellae (higher T_m). These lamellae initiate spherulitic growth. The small grains that are formed during injection from the high temperature are neither strong nor able to initiate spherulitic growth.

5 Conclusion

By in-situ monitoring of the nanostructure evolution in 3 differently processed TPU samples during straining experiments mechanisms have been revealed that cause different mechanical properties in the material. WAXS monitoring carried out on samples freshly prepared from extruded granules as compared to matured samples from crushed granules used in the SAXS study show that aging (and chain decomposition) is a problem in the study of this TPU material so that not all results of the WAXS study can be used to better understand the mechanisms that govern the macroscopic mechanical properties on the nanometer and on the sub-nanometer scale. Nevertheless, the WAXS experiments show that the material does not develop crystallites big enough to be detected by WAXS. Moreover, a new method for the detection of chain-orientation mechanisms based on the analysis of the derivative $d f_{or}/d\varepsilon$ of the uniaxial orientation parameter $f_{or}(\varepsilon)$ appears to be suitable for application in follow-up studies. Compared to published technique in studies of TPUs we have combined several achievements by other groups and advanced the technique ourselves. For instance, the WAXS data are mapped into reciprocal space before the analysis, and diffuse background scattering is subtracted before pole figures are analyzed. The local macroscopic strain at the point of X-ray irradiation is determined and the change of the sample cross section is considered in the computation of the stress. The straining is not carried out step-wise, but continuously. Unfortunately the strain rate is still very low, because sufficient signal-to-noise ratio is required for the CDF analysis. The corresponding limit will be shifted towards shorter exposure and faster straining, as soon as much more brilliant synchrotron beam lines and fast detectors will be generally accessible. Because many TPU materials are changing their properties with time, it would be a big progress if 2D SAXS and WAXS could be monitored simultaneously.

Acknowledgment. The authors thank the Hamburg Synchrotron Radiation Laboratory (HASYLAB) for beam time granted in the frame of project II-20080015.

References

[1] R. Bonart, *Angew. Makromol. Chem.* **1977**, *58*, 259.
[2] A. J. Ryan, M. J. Elwell, W. Bras, *Nuclear Instr. Meth. Phys. Res.* **1995**, *B97*, 216.
[3] G. Pompe, A. Pohlers, P. Pötschke, J. Pionteck, *Polymer* **1998**, *39*, 5147.
[4] A. Frick, A. Rochman, *Polymer Testing* **2004**, *23*, 413.
[5] A. Frick, M. Mikoszek, *Macromol.Symp.* **2010**, *294*, 102.
[6] H. J. Qi, M. C. Boyce, *Mech. Mat.* **2005**, *37*, 817.
[7] R. Bonart, *J. Macromol. Sci. Part B* **1968**, *2*, 115.
[8] R. Bonart, *Kolloid Z. u. Z. Polymere* **1966**, *211*, 14.
[9] H. Meyer, R. Bonart, *Prog. Colloid Poly. Sci.* **1985**, *71*, 103.
[10] R. Bonart, F. Bötzl, J. Schmid, *Makromol. Chem.* **1987**, *188*, 907.
[11] P. R. Laity, J. E. Taylor, S. S. Wong, P. Khunkamchoo, K. Norris, M. Cable, G. T. Andrews, A. F. Johnson, R. E. Cameron, *Polymer* **2004**, *45*, 5215.
[12] P. R. Laity, J. E. Taylor, S. S. Wong, P. Khunkamchoo, M. Cable, G. T. Andrews, A. F. Johnson, R. E. Cameron, *Macromol. Mater. Eng* **2006**, *291*, 301.
[13] R. S. Waletzko, T. J. K. LaShanda, B. D. Pate, E. L. Thomas, P. T. Hammond, *Macromolecules* **2009**, *42*, 2041.
[14] D. J. Blundell, G. Eeckhaut, W. Fuller, A. Mahendrasingam, C. Martin, *J. Macromol. Sci. Part B* **2004**, *43*, 125.
[15] N. Stribeck, *J. Macromol. Sci. Part C: Polymer Reviews* **2010**, *50*, 40.
[16] C. Martin, G. Eeckhaut, A. Mahendrasingam, D. J. Blundell, W. Fuller, R. J. Oldman, S. J. Bingham, T. Dieing, C. Riekel, *J. Synchr. Rad.* **2000**, *7*, 245.

[17] N. Stribeck, U. Nöchel, S. S. Funari, T. Schubert, A. Timmann, *Macromol. Chem. Phys.* **2008**, *209*, 1992.
[18] Z. Denchev, N. Dencheva, S. S. Funari, M. Motovilin, T. Schubert, N. Stribeck, *J. Polym. Sci. Part B: Polym. Phys.* **2010**, *48*, 237.
[19] N. Stribeck, “Downloads”, http://www.chemie.uni-hamburg.de/tmc/stribeck/dl, **2008**.
[20] VNI, “PV-WAVE manuals”, V 7.5, Houston, TX, USA, **2007**.
[21] M. Polanyi, *Z. Phys.* **1921**, *7*, 149.
[22] N. Stribeck, *Acta Cryst.* **2009**, *A65*, 46.
[23] M. Lorenz, K. C. Holmes, *J. Appl. Cryst.* **1993**, *26*, 82.
[24] G. Rajkumar, H. AL-Khayat, F. Eakins, A. He, C. Knupp, J. Squire, *Fibre Diffraction Rev.* **2005**, *13*, 11.
[25] W. Bian, H. Wang, I. McCullough, G. Stubbs, *J. Appl. Cryst.* **2006**, *39*, 752.
[26] N. Stribeck, U. Nöchel, *J. Appl. Cryst.* **2009**, *42*, 295.
[27] W. Ruland, *Acta Cryst.* **1961**, *14*, 1180.
[28] P. H. Hermans, P. Platzek, *Kolloid-Z.* **1939**, *88*, 68.
[29] I. M. Ward, Ed. *Structure and Properties of Oriented Polymers*, Chapman and Hall, London, **1997**.
[30] N. Stribeck, *X-Ray Scattering of Soft Matter*, Springer, Heidelberg, New York, **2007**.
[31] C. H. Reinsch, *Numer. Math.* **1971**, *16*, 451.
[32] H. Koerner, R. A. J. J. Kelley, Vaia, *Macromolecules* **2008**, *41*, 4709.
[33] N. Stribeck, *J. Appl. Cryst.* **2001**, *34*, 496.
[34] N. Stribeck, A. Almendarez Camarillo, U. Nöchel, C. Schroer, M. Kuhlmann, S. V. Roth, R. Gehrke, R. K. Bayer, *Macromol. Chem. Phys.* **2006**, *207*, 1239.
[35] P. Debye, A. M. Bueche, *J. Appl. Phys.* **1949**, *20*, 518.
[36] G. Porod, *Colloid Polym. Sci.* **1951**, *124*, 83.
[37] C. G. Vonk, *J. Appl. Cryst.* **1973**, *6*, 81.
[38] F. J. Baltá Calleja, C. G. Vonk, *X-Ray Scattering of Synthetic Polymers*, Elsevier, Amsterdam, **1989**.
[39] W. Ruland, *Colloid Polym. Sci.* **1977**, *255*, 417.
[40] C. G. Vonk, *Colloid Polym. Sci.* **1979**, *257*, 1021.
[41] M. F. Sonnenschein, Z. Lysenko, D. A. Brune, B. L. Wendt, A. K. Schrock, *Polymer* **2005**, *46*, 10158.
[42] A. Saiani, W. A. Daunch, H. Verbeke, J. W. Leenslag, J. S. Higgins, *Macromolecules* **2001**, *34*, 9059.
[43] P. Pötschke, L. Häußler, S. Pegel, R. Steinberger, G. Scholz, *Kautschuk Gummi Kunststoffe* **2007**, *60*, 432.
[44] C. D. Eisenbach, H. Nefzger, H. Hayen, V. Enkelmann, *Macromol. Chem. Phys.* **1994**, *195*, 3325.
[45] R. H. Somani, B. S. Hsiao, A. Nogales, S. Srinivas, A. H. Tsou, I. Sics, F. J. Baltá Calleja, T. A. Ezquerra, *Macromolecules* **2000**, *33*, 9385.
[46] Z.-G. Wang, Z.-Y. Xia, Z.-Q. Yu, E.-Q. Chen, H.-J. Sue, C. C. Han, B. S. Hsiao, *Macromolecules* **2006**, *39*, 2930.
[47] C. B. Wang, S. L. Cooper, *Macromolecules* **1983**, *16*, 775.
[48] K. Hoffmann, R. Bonart, *Makromol. Chem.* **1983**, *184*, 1529.
[49] G. M. Estes, R. W. Seymour, S. L. Cooper, *Macromolecules* **1971**, *4*, 452.
[50] G. L. J. C. Moreland, Wilkes, R. B. Turner, *J. Appl. Polym. Sci.* **1991**, *43*, 801.
[51] Z. W. Wilchinsky, *J. Appl. Phys.* **1960**, *31*, 1969.
[52] W. Ruland, H. Tompa, *Acta Cryst.* **1968**, *A24*, 93.
[53] W. Ruland, H. Tompa, *J. Appl. Cryst.* **1972**, *5*, 225.
[54] W. Ruland, *Colloid Polym. Sci.* **1977**, *255*, 833.
[55] P. Ianelli, *J. Appl. Cryst.* **1994**, *27*, 1055.
[56] A. Peterlin, *J. Mater. Sci.* **1971**, *6*, 490.
[57] A. Peterlin, *Text. Res. J.* **1972**, *42*, 20.
[58] G. Porod, *Fortschr. Hochpolym.-Forsch.* **1961**, *2*, 363.
[59] N. Stribeck, *ACS Symp. Ser.* **2000**, *739*, 41.

Synopsis. Injection molded TPU (sealing-grade) studied by 2D SAXS exhibits a simple "sandwich" (hard-soft-hard) domain structure. The chart shows shape distributions of “hard+soft” domains during straining. The lengthening is highly non-affine. Simple analysis reveals nanostructure evolution mechanisms as a function of processing temperature of the melt. At 235 °C soft material with weak hard domains is made.